Spreading of a thin two-dimensional strip of fluid on a vertical plane: Experiments and modeling

A. G. González,* J. Diez,† J. Gomba,‡ and R. Gratton†
Instituto de Física Arroyo Seco, Universidad Nacional del Centro de la Provincia de Buenos Aires, Pinto 399, 7000 Tandil, Argentina

L. Kondic
Department of Mathematical Sciences and Center for Applied Mathematics and Statistics, New Jersey Institute of Technology, Newark, New Jersey 07102, USA

(Received 3 October 2003; revised manuscript received 20 February 2004; published 30 August 2004)

We study the thin-film flow of a constant volume of silicon oil (polydymethilsiloxane) spreading down a vertical glass plate. The initial condition is generated from a horizontal fluid filament of typical diameter 0.4 mm. Two optical diagnostic methods are used: One based on an anamorphic system, and the other on the Schlieren method. The first one allows for a detailed characterization of the early stable stage of the spreading which is used to estimate the thickness of the precursor film needed to model the flow. The second one captures the bidimensional pattern of the transversal film instability. We use these techniques to determine the film thickness profiles, and the evolution of the moving contact line, including its shape and Fourier spectra. The numerical simulations of the stable stage of spreading are in good quantitative agreement with the experimental results. We develop a model based on linear stability theory that predicts the evolution of the modes present in the linear stage of the instability.

DOI: 10.1103/PhysRevE.70.026309 PACS number(s): 47.20.−k, 68.15.+e, 47.15.Gf

I. INTRODUCTION

The scenario where a solid surface is being coated by a thin liquid film is ubiquitous in nature, and it also appears in a variety of technological problems (microchip production and microfluidic devices). Basically, the coating process develops as a balance between viscous and surface tension forces plus possibly a body force. The latter is often the main driving force and, depending on the configuration, it may be represented by gravity force [1,2], centrifugal force [3,4], or thermocapillary force [5–7]. Coating flows exhibit two main features: One is the existence of a free surface, whose position must be calculated as a consequence of the balance among the acting forces, and the other one is the presence of a contact line, which defines the boundary between the film (bulk) and the uncoated surface. The combination of these two features may give place to complex topologies of stable or unstable flows, with nontrivial shapes of the free surface and corrugations of the contact line.

Here, we concentrate on the case of a thin film flowing down a vertical planar substrate. In particular, we consider the constant volume (CV) situation, in which a two-dimensional fluid strip is placed at the top of the plane. Previously reported experiments have shown that after some time the initially straight advancing front line, where the liquid, gas, and solid phases meet, becomes unstable with respect to perturbations along the strip. It is generally accepted that this instability is related to the formation of a capillary ridge just behind the advancing contact line. However, the analysis of the instability has only been done for the constant flux (CF) case, in which the fluid thickness far behind the contact line is kept constant (thus providing an unlimited supply of fluid). In this case, the analysis exploits a key feature of the CF flow, namely, the translational invariance which allows for the existence of a traveling wave solution. In contrast, the CV case loses this property and then the analysis presents additional difficulties, as outlined below. Thus, it is still not clear what determines the long-time nature of the instability, in particular the main features of the final patterns, such as their distances and the shapes.

In recent years, many researchers have paid attention to this problem. On the experimental side, except for the work by Johnson [8,9], most of the authors have considered the CV case [1,10–12]. This is understandable considering that the CF case involves a more complex setup in order to assure the constant fluid inflow. It must be noted that in the CV case, rather than the fluid volume, the cross-sectional area of the initial condition is the characteristic parameter of the flow. The transversal extension is irrelevant since it is usually much larger than the flow extension in the streamwise direction. In contrast to above mentioned experiments for the CV case, here we use much smaller areas, and thus the fluid spreads as a micrometric film. As a consequence, the flow studied here is more representative of the coating processes used in applications, and the corresponding experimental results are then also of particular interest to this field. Moreover, the lubrication theory is valid to a high degree of accuracy for such thin films. For example, the possibility of rolling motion at the advancing fronts [12], that may occur for thicker (millimetric) films, is surely ruled out in the present experiments.

The initial condition is a horizontal viscous filament [polydymethilsiloxane (PDMS) oil of cross section A of the order of 10^{-4} cm^2] placed near the top of a vertical glass plate, which spreads down the plane under complete wetting

*Also at: CONICET, Argentina. Electronic address: aggonzal@exa.unicen.edu.ar
†Also at: CONICET, Argentina.
‡Also at: CONICET, Argentina.

conditions. As the initially straight front line advances, it becomes corrugated and, after some time, the flow evolves by forming well-defined rivulets (called fingers) separated by troughs.

The main goal of this work is to achieve a quantitative description of the spreading by performing controlled experiments, detailed optical diagnostics, and numerical simulations in a coordinated fashion. This description is necessary to test the validity of the assumptions made in the usual modeling of the flow. One of these assumptions is the existence of an ultrathin precursor film at the moving contact line. An experimental issue is that the setups commonly used to detect and measure the precursor film [13] preclude the study of the global spreading dynamics. Instead, in this work, we indirectly determine the precursor film thickness, h_f, that quantitatively describes the macroscopic flow, and we also measure the evolution of the free surface. Regarding the unstable stage of the spreading, a detailed study of the spatial spectra of the contact line as done in this work is needed to validate the theories and numerical simulations performed to understand the mechanisms involved in the development of the instability.

We use two simultaneous optical techniques to analyze the problem. The first one (Sec. III A) is based on the use of an anamorphic lens which processes a vertical light sheet that passes through the flow region. This technique allows one to obtain the thickness profile from which we accurately determine the area, A (for the early stable stage), and thus the volume of the fluid. By using these profiles and the evolution of the width of the fluid strip, we determine the value of the precursor film thickness needed to perform numerical simulations which quantitatively account for real situations. The other technique (Sec. IV A) consists of a Schlieren method with an iris diaphragm stopping the deflected rays of an illuminating parallel beam. This method produces images which show most of the relevant features of the instability, such as the shape of the contact line and the free surface topography. In particular, from digitized pictures, we obtain for the first time the evolution of the Fourier spectrum of the contact line at the fluid front (front line). In Sec. V, we develop a semianalytical model that predicts the value of the dominant wavelength of the spatial front lines' spectrum. The results of this model are in very good agreement with the experimental time evolution of the spectrum in the linear stage of the instability, and the model also predicts the growth rates of the normal modes.

II. BASIC DESCRIPTION OF CONSTANT VOLUME PROBLEM

The initial fluid configuration is a vertical filament flowing out from a small nozzle at the bottom of a vessel filled with silicon oil [see Fig. 1(a)]. Both the nozzle diameter and the fluid properties allow one to control the value of the area A of the filament. The lower limit of the attainable A's is given by the Rayleigh instability of the jet which may lead to the formation of beads for small enough radius. We use PDMS with kinematic viscosity $\nu = 20$ St, density $\rho = 0.96$ g cm^{-3}, and surface tension $\gamma = 19.8$ dyn/cm, so that

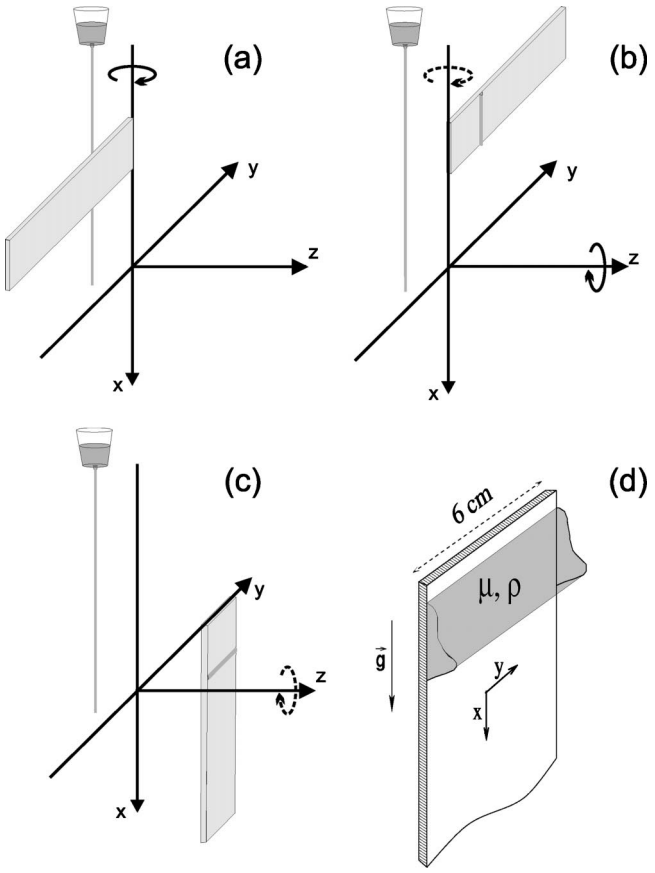

FIG. 1. Sketch of the mechanical system to place the fluid on the substrate. (a) Initial setup and capture of the filament by the substrate. (b) Filament on the substrate and intermediate position (dashed arrows indicate previous rotation). (c) Final position. (d) Sketch of the constant volume spreading down the vertical substrate.

the capillary length is $a = \sqrt{(\gamma/\rho g)} = 0.145$ cm.

The filament is captured on a glass (6 cm wide) by performing suitable rotations of its frame before reaching the final vertical position [see Figs. 1(b) and 1(c)]. All of these movements take about 1–2 s, i.e. a time interval which is very short compared to the time scale of the experiment (see below). In order to obtain a good horizontal positioning of the fluid strip, it is necessary to carefully control the directions of the rotating shafts. The mechanical adjustments are optically checked by analyzing a digitized Schlieren image of the spreading (see Sec. IV A for details). This experimental procedure allows one to obtain a fluid strip with contact lines which are both horizontal and straight, so that the initial configuration has a constant cross-sectional area along the y direction [see Fig. 1(d)]. After each experiment, the oil is removed and the glass is cleaned by immersion in a bath of sulphochromic acid for several days, in order to ensure the removal of any oil residual on the glass surface. Before a new experiment, the glass is washed with distilled water and dried with hot air.

In the following sections, we show that both contact lines (rear/upper and frontal/lower ones) remain straight during an early stage of the experiment. At this stage, due to capillary effects, the rear line climbs uphill a short distance (much

smaller than the width of the film in the streamwise direction), while the front moves downhill significantly. These movements are concurrent with a deformation of the shape of the cross section. A second stage starts when the frontal contact line appreciably departs from the straight line shape. Later on, experiments show the growth of corrugations which evolve into a pattern of rivulets (or fingers).

We have implemented two optical techniques in order to observe and probe the relevant features of the flow in both stages. One of these techniques is aimed at measuring the thickness profile of the spreading as well as the position of both contact lines. During the early stage, this technique allows an accurate determination of the fluid volume. The other one is intended to describe the topography of the free surface and also the irregular shape of the contact line.

Usually, this type of flow is studied within the lubrication approximation, i.e., small Reynolds number and small free surface slope. These hypotheses are satisfied in our experiments since PDMS oil is very viscous, and the strip is of a small aspect ratio (typically, height/width <0.1). Thus, under the action of gravity and surface tension, the governing equation for the fluid thickness $h(x,y,t)$ is [14]:

$$3\mu\frac{\partial h}{\partial t} + \gamma\nabla\cdot(h^3\nabla(\nabla^2 h)) + \rho g\frac{\partial h^3}{\partial x} = 0, \qquad (1)$$

where $\mu=\nu\rho$ is viscosity, and g is gravity. The three terms in Eq. (1) stand for the viscous, capillary, and gravitational forces, respectively. Here, x is the downhill coordinate.

Equation (1) includes the nonslip boundary condition at the substrate surface. Due to the well-known contact line paradox (macroscopic divergence of the viscous dissipation rate), all theoretical and computational methods require some regularizing mechanism: Either assuming the existence of a thin precursor film of thickness h_f in front of the apparent contact line [2,15,16], or relaxing the no-slip boundary condition at fluid–solid interface [14,17,18] by introducing a slipping length l_s. We have performed an extensive comparison of these regularizing mechanisms applied to the spreading drop problem [19]. In that paper, it is shown that the precursor film model leads to the results that are very similar to the ones obtained using slip model for $h_f \approx l_s$. Since the computational performance of the precursor model is much better, we use this model as a regularizing method in this work.

We have recently developed a numerical method [20] to solve Eq. (1), and used it to analyze the pattern formation in CF flows [21–23]. Nevertheless, we report here only the results of one-dimensional numerical simulation that study the y-independent stage of the flow. We leave the comparison of the y-dependent numerical solutions of Eq. (1) with CV experiments for a forthcoming paper.

Within the framework of a precursor film model, a certain value of h_f must be assumed in order to perform the numerical simulations. Typically, one chooses h_f to be one or two orders of magnitude smaller than the average bulk thickness. However, in order to produce results in *quantitative* agreement with the experiments, we must first determine the appropriate value of h_f that reflects the actual physics of the contact line. This is done in the following section by comparing numerical results for different values of h_f with the experimental thickness profiles for a given area A. Most importantly, the resulting value turns out to be independent of A. Therefore, the simulations that we perform to describe other experiments for different areas using the same h_f also lead to very good agreement.

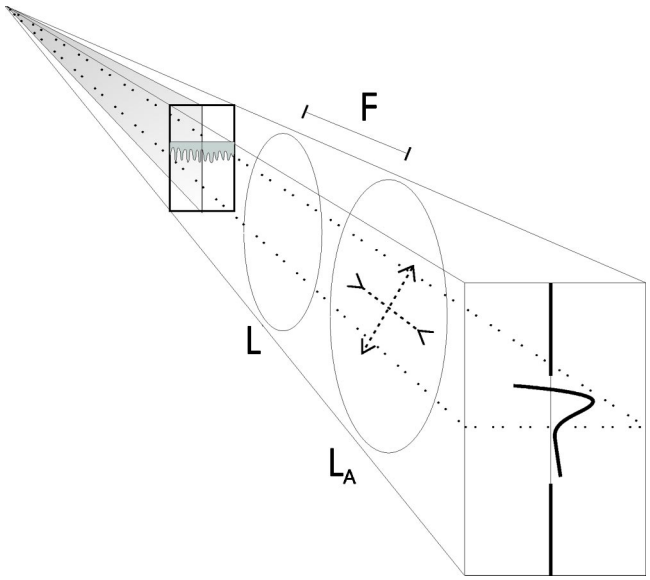

FIG. 2. Scheme of the anamorphic system.

III. STABLE STAGE

A. Anamorphic lens technique

The early stages of the spreading, when h is almost independent of the transverse (horizontal) y coordinate, are studied by employing the optical system reported by Thomas *et al.* [24]. The liquid film is probed by a parallel light sheet along the (vertical) x direction impinging perpendicular to the glass substrate. A lens L of focal length $F=20.1$ cm forms a magnified image of the spreading region with a magnification factor $M=6.25$ (see Fig. 2). Then, at the focal plane of L, we place an anamorphic lens, L_A, equivalent to two crossed cylindrical lenses (one convergent and the other divergent) with focal lengths of an equal magnitude $f=120$ cm, and their axes at $\pm 45°$ with respect to the x axis (a cylindrical–spherical ophthalmic lens, conveniently chosen and oriented, does this job). Therefore, a bright curve $y_s(x_s)$ appears on the screen, whose coordinates satisfy:

$$x_s = Mx, \quad y_s = M\frac{F^2}{f}(n-1)\frac{\partial h}{\partial x}, \qquad (2)$$

where $n=1.4$ is the refraction index of the silicon oil, and we have assumed that the y gradients of h are negligible. Therefore, this technique is particularly valuable as a tool to analyze the early stages of the spreading. In later stages, the method becomes more difficult to use due to the presence of transverse gradients, except in particular positions with high symmetry, such as troughs or fingers. In fact, we will show

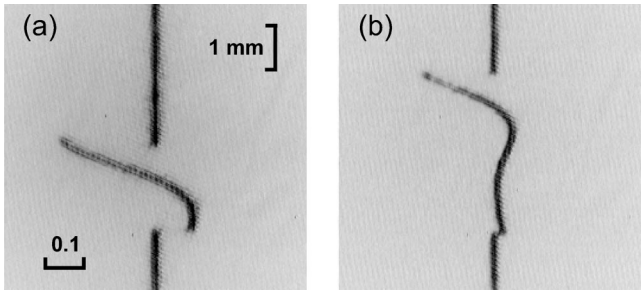

FIG. 3. Snapshots of the originally vertical light sheet after being refracted by the spreading and deflected by the anamorphic system for $A=6.75\times10^{-4}$ cm^2. The thickness gradients along the line are responsible for the horizontal deflections. (a) $t=1.97$ min, (b) $t=20.07$ min. The vertical segment shows the spatial scale at the substrate, and the horizontal one corresponds to the scale of $\partial h/\partial x$.

thickness profiles in the following section along these particular lines.

In Fig. 3, we show two images of the observed curve $y_s(x_s)$. They correspond to early stages of the spreading of a filament with an approximate diameter of 0.4 mm placed initially near the top of the vertical glass. Images are inverted upside down by the optical system, so that the upper discontinuity corresponds to the front falling down, and the lower discontinuity represents the rear front. According to Eq. (2), the amplitude of the curve, y_s, is related to the slope of the thickness profile. Clearly, the steepest slope is at the front falling down (dynamic contact angle). The right and left deflections indicate that there are zones with slopes of opposite sign and, as a consequence, a point of zero slope (maximum thickness). Figure 3(a) corresponds to an almost symmetric early configuration, while Fig. 3(b) shows two distinguishable regions: One around the zero slope point (bump region) and the other in the rear, where the slopes are much smaller.

According to Eq. (2), an integration of the curve $\partial h/\partial x$ versus x yields the thickness profile $h(x)$, and a further integration gives the area, A. Since the optical technique assumes a paraxial approximation for the rays of the light sheet, the contact line region must be considered in more detail. In this zone, the steepness of the profile produces a much greater deviation angle than in the rest of the film. If the assumed approximation fails, the end of the deflected curve is displaced in the vertical x direction with respect to the corresponding end of the straight line. Thus, a gap or an overlapping might appear on the screen. Although this effect does not alter the determination of the width of the film, the uncertainty in the values of the slopes close to this critical region affects the calculation of A. This effect becomes more critical as A increases, posing a limit to the method. We pay special attention to minimize this problem by a careful positioning of the anamorphic lens, and when processing the digitized images.

B. Experimental results and comparison with numerical simulations

A crucial element in reaching not only qualitative, but also quantitative agreement between experiment and theory is using an appropriate value of the precursor film thickness, h_f. As mentioned in Sec. I, this film is very thin and therefore its measurement requires a technique, such as ellipsometry [13], which is not compatible with our probing methods to measure the macroscopic flow. To circumvent this difficulty, we perform numerical simulations of the y-independent version of Eq. (1). Clearly, this approach requires very careful and well resolved computations, since a very thin precursor film also demands a very small computational step size, Δx, in order to achieve numerical convergence. However, as we will see below, the use of the correct h_f in this work leads to full agreement between computed and measured time scales, therefore eliminating the need for time-scale adjustment [25,26].

We obtain h_f by performing an iterative procedure. First, we choose two experimental thickness profiles, one close to the beginning of the spreading (t_a), and the other at a later time t_b (chosen small enough to ensure that the front is not yet corrugated). Then, we use the experimental profile at t_a as an initial condition in the numerical simulation, and we integrate it forward in time using appropriate initial guess for h_f. We then compare the computed and the experimental profile at t_b. Based on the difference between these two profiles, we choose the next iterate for h_f and repeat this procedure until convergence. The result of this iterative procedure is the value of h_f which produces very good *quantitative* agreement between computed and observed profiles: $h_f=43$ nm (or $h_f=3\times10^{-5}a$). Such a small value also requires very well resolved computations: We find that the results are fully converged for $\Delta x=10^{-3}a$. We have also verified that this value of h_f remains unchanged if we choose a different t_b. We note that this h_f is in the range of the thicknesses measured and reported in literature for precursor films [27,28]. From now on, we use this value for the comparisons between experiments and simulations performed using different fluid cross-sectional areas.

In Fig. 4, we show the experimental results for $A=6.75\times10^{-4}$ cm^2 (black dots). The evolution of the thickness profile starts with a shape resembling a cylindrical cap whose maximum is moving downward [see Fig. 4(a)]. During this stage, the front line is practically straight. Later on, we observe the appearance of two regions [see Figs. 4(b) and 4(c)]: the rear region, which acquires an almost parabolic shape, and the front region which evolves by developing a large bump. Once this structure is formed, corrugations of the front line may start developing (see Sec. V). Figure 4(c) shows a well developed profile when the front line is about to start corrugating. Note that in this stage, the regions mentioned above are connected by a zone of almost flat thickness ("plateau"). Similar profile evolution is also observed in the experiments carried out by Tanner [29]. He obtained the profiles by scanning a two-dimensional droplet with a light beam. However, his method yields only around ten points per profile, whereas our technique probes the fluid instantaneously and provides a continuous (surface slope) curve.

The gray lines in Fig. 4 correspond to the numerical simulations. We see that the results are in excellent agreement with the experimental data. The simulations are performed starting from the initial condition (cylindrical cap),

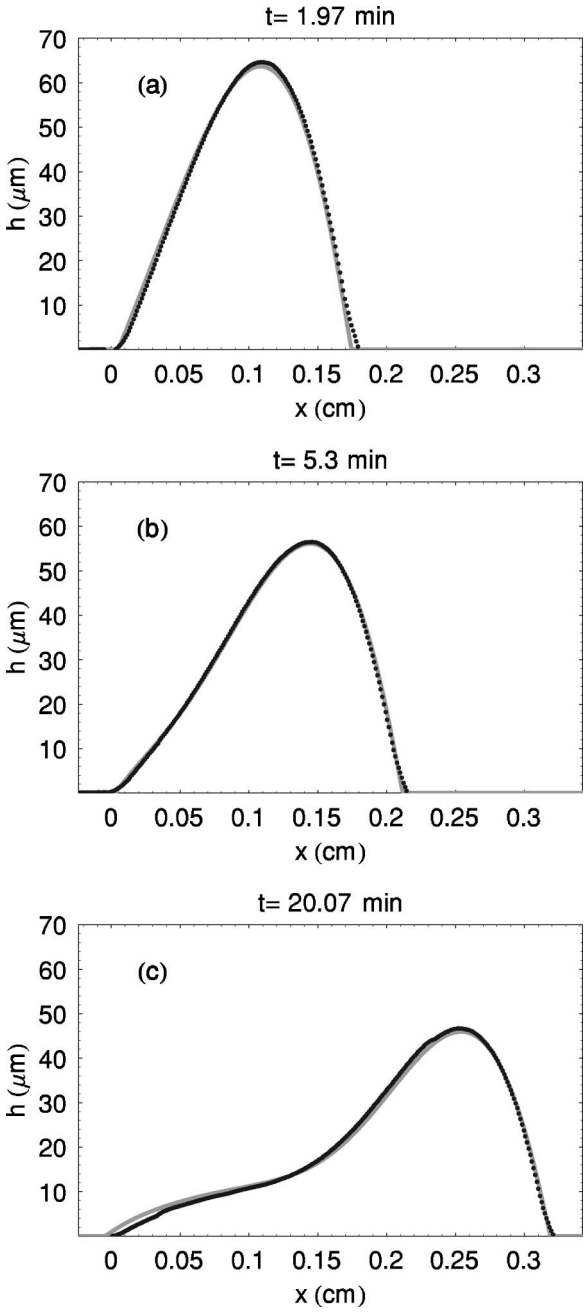

FIG. 4. Thickness profiles for $A=6.75\times10^{-4}$ cm^2 for different times. Black dots correspond to experimental data and the gray lines to the numerical simulations with $h_f=3\times10^{-5}a$.

$$h(x,0)=h_0\left[1-\left(\frac{x}{w_0/2}\right)^2\right], \tag{3}$$

where $w_0=w(0)$ is the width of the strip in the streamwise direction at $t=0$, and h_0 is its maximum thickness. Since both the values of w_0 and the area A are given by the anamorphic technique, we calculate h_0 as $h_0=3A/2w_0$. We have verified that this initial shape leads to results that are in full agreement with those obtained by using an experimental profile for a given $t>0$. Therefore, we use the initial condition as given by Eq. (3) for all the simulations that follow.

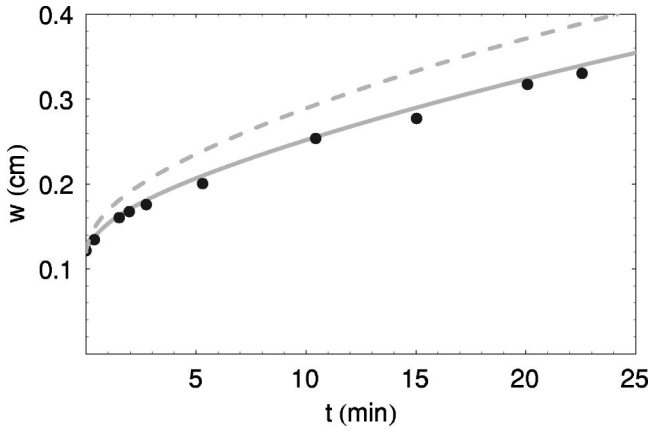

FIG. 5. Comparison of the width of the film between experiments (black dots) and numerical simulations for $h_f=3\times10^{-5}a$ (gray solid line) and $h_f=3\times10^{-4}a$ (gray broken line) for $A=6.75\times10^{-4}$ cm^2.

The comparison of the numerical width of the film (solid gray line) with the experimental results (black dots), $w(t)$, is shown in Fig. 5. We define

$$w=x_f-x_r, \tag{4}$$

where x_f, x_r are the positions of the front and rear contact lines, respectively. We use the width, w, instead of x_f in order to consider a quantity independent of the reference frame (except for the very first stages, x_r does not vary appreciably during the spreading). In order to show the sensitivity of the simulations with respect to the precursor film thickness, we also show in Fig. 5 the numerical width obtained with $h_f=3\times10^{-4}a=430$ nm (dashed gray line). Even though this value is still within the range expected for a precursor film, we clearly see that the predicted behavior of $w(t)$ strongly differs from experiments, while the results for $h_f=43$ nm are in very good agreement.

We have carried out a series of experiments with A's ranging from 3×10^{-4} to 15×10^{-4} cm^2. In order to show the characteristic features of the problem, we discuss here only two more cases, one for a larger area, and another for a smaller one. The general behavior of all other experiments is similar to that of these three examples.

The results for a larger area ($A=10.3\times10^{-4}$ cm^2) are shown in Figs. 6–8. We observe that the numerical results obtained by using the value of h_f determined for the case $A=6.75\times10^{-4}$ cm^2 also show very good agreement for these experiments. As mentioned above, for a large area, we expect some effects related to the presence of higher slopes at the moving contact line. In fact, the overlapping at the upper discontinuity in Fig. 6(a) is due to this effect. This deviation from the expected behavior affects only a small portion of the curve, and does not modify the precision of the rest of it. Upon integration, we minimize the contribution from that region in order to obtain a reliable thickness profile. Note that the overlapping diminishes as time progresses [see Fig. 6(b)], because the dynamic contact angle is lower at this later time. In practice, we calculate the profiles and their corresponding areas at several time instances, and find that the

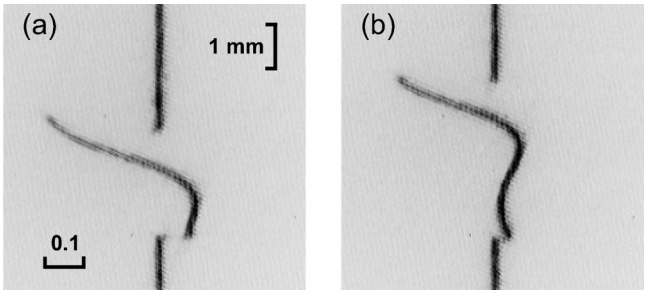

FIG. 6. Snapshots of the originally vertical light sheet after being refracted by the spreading and deflected by the anamorphic system for $A=10.3\times10^{-4}$ cm^2. The thickness gradients in the direction of spreading generate the horizontal deflections of the line. (a) $t=2.23$ min, (b) $t=8.7$ min.

measured areas have a fluctuation which is at most 5%. Then, the reported value of A is obtained by performing an appropriate average. Naturally, we do not use this procedure for times too close to the onset of the instability, since the assumption of constant cross section no longer holds. We verify that an area calculated for a certain time corresponds to the stable stage by simultaneously observing the shape of the front line for that time (see Sec. IV A).

A feature of this experiment ($A=10.3\times10^{-4}$ cm^2) is that the flow evolution is much faster than the previous case where A is smaller. Note that formation of the structure composed of a bump region and a parabolic rear region occurs now for times as early as ≈5 min [see Fig. 7(b)] compared with 20 min in the smaller area case [see Fig. 4(c)].

Figure 9 shows a typical case of one of the smallest areas studied in this work, $A=3.6\times10^{-4}$ cm^2. Though there is no overlapping now, the main difficulty here is the smallness of the deviation of the light beams. Since for late times [Fig. 9(b)], the mean amplitude of the deviation becomes comparable with the thickness of the line, the relative error introduced by this effect is more important than in the previous cases. In all experiments, we determine the curve from the average of the horizontal positions of the pixels weighted with their intensities. This procedure yields the coordinates of a one-pixel line, which minimizes the just mentioned effect.

Figures 10 and 11 show that the numerical simulations, performed with the same h_f as before, are also in good agreement with this experiment. Note that the small differences in the thickness profiles are not larger than 2 μm. The fact that a single value of h_f allows one to adjust the calculations to experiments in a significant range of areas, is consistent with the assumption that h_f is a characteristic feature of the particular interaction between our PDMS and the glass substrate, and it does not depend on the amount of spreading fluid.

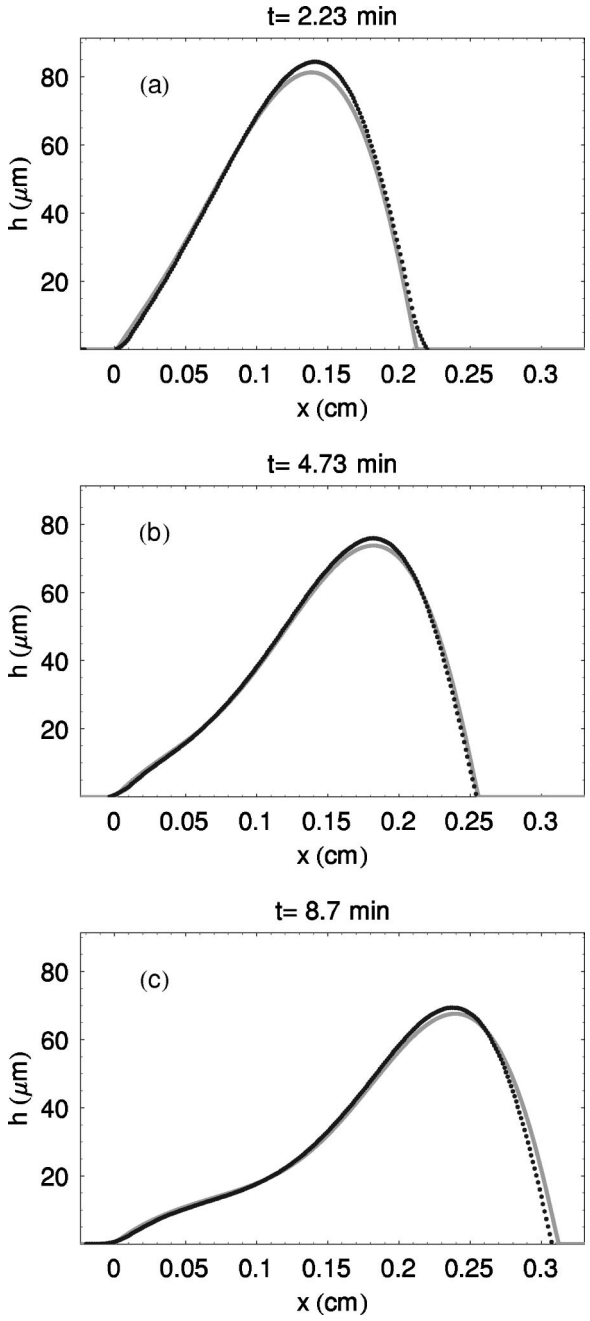

FIG. 7. Thickness profiles for $A=10.3\times10^{-4}$ cm^2 for different times. Black dots correspond to experimental data and the gray lines to the numerical simulations with $h_f=3\times10^{-5}a$.

IV. UNSTABLE STAGE

A. Schlieren method

In addition to the previous technique, we also use a Schlieren method to probe the spreading. A sliding mirror allows one to switch between one technique and the other. The Schlieren technique is used with a diaphragm centered at the focus of lens L (see Fig. 2) and an expanded probing laser beam. This expansion is achieved by a collimating system which includes a pinhole for spatial filtering. This system generates a 6 cm wide beam of parallel rays, which illuminates the substrate from behind. The setup is adjusted to produce an illumination as uniform as possible.

The images thus obtained show a pattern of dark and bright zones, which correspond to regions where the modulus of the gradient of the thickness is greater or smaller than a cutoff value, respectively. The cutoff varies with the diam-

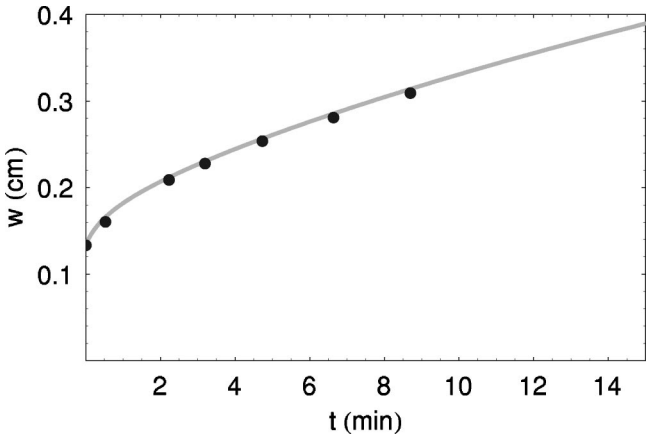

FIG. 8. Comparison of the width of the film between experiments (black dots) and numerical simulations with $h_f=3\times10^{-5}a$ (gray lines) for $A=10.3\times10^{-4}$ cm^2.

eter d of the diaphragm (all photos presented here have $d\approx1$ mm). From these patterns, it is possible to reconstruct the thickness of the film. The results of this procedure and the comparison with the numerical solution of Eq. (1) will be reported in a forthcoming paper. In this work, we restrict our analysis to the study of the shape of the front line. Figure 12 shows four typical images obtained by using this technique for area $A=6.75\times10^{-4}$ cm^2 (the images are inverted by the optical system). We clearly see the formation of a pattern of fingers and troughs. In order to obtain a well resolved shape of the front line, we filter the Schlieren image to correct the remaining lack of uniformity in the illumination. Then, we increase the contrast of the image and obtain the coordinates of hundreds of pixels corresponding to the front line.

B. Unstable contact line: Spectra, fingers, and troughs

The analysis of the instability pattern is performed by calculating the discrete Fourier transform (DFT) of the front lines. Here, we employ the following definition to make this transformation:

$$v_s=\frac{1}{\sqrt{n}}\sum_{r=1}^{n}u_r\exp[2\pi\imath(r-1)(s-1)/n], \tag{5}$$

where n is the number of sampling points with x coordinates u_r, r denotes the y ordering of the pixel, and s is an integer

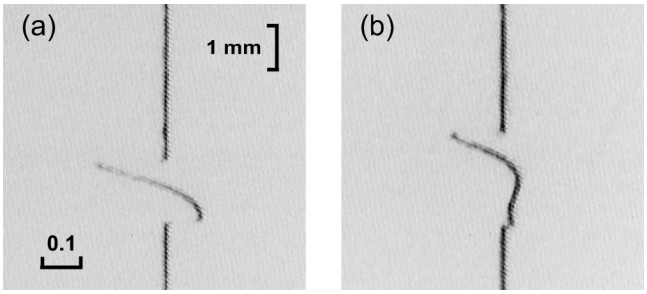

FIG. 9. Snapshots of the originally vertical light sheet after being refracted by the spreading and deflected by the anamorphic system for $A=3.6\times10^{-4}$ cm^2. The thickness gradients in the direction of spreading generate the horizontal deflections of the line. (a) $t=2.53$ min, (b) $t=18.1$ min.

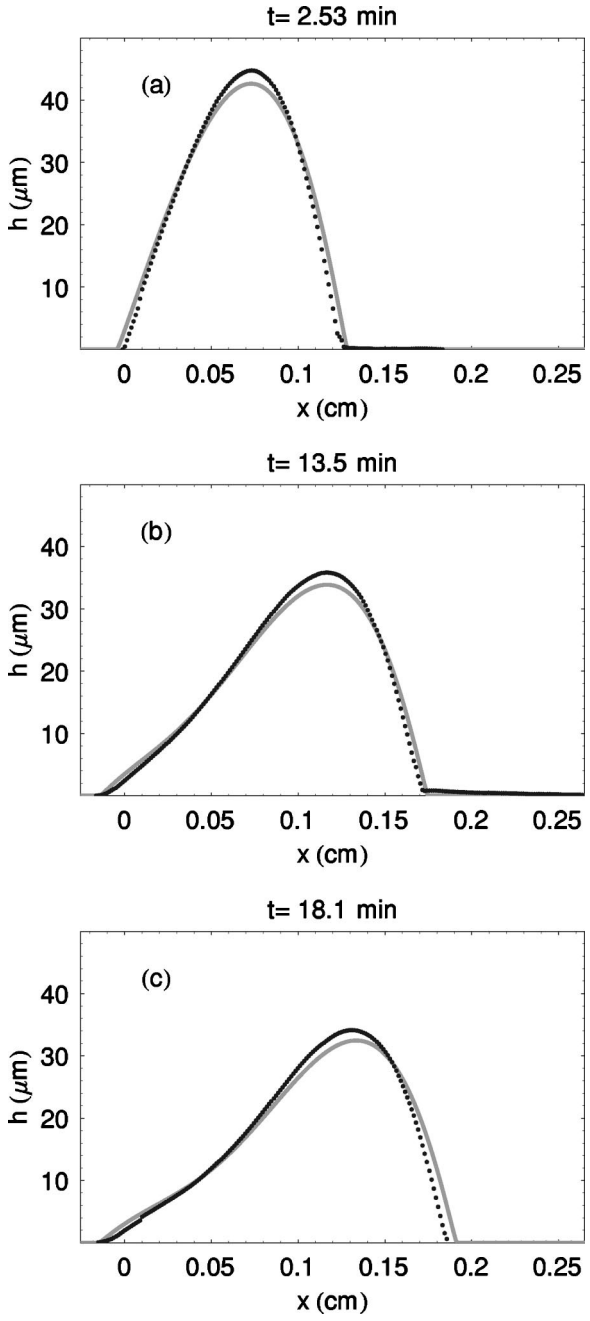

FIG. 10. Thickness profiles for $A=3.6\times10^{-4}$ cm^2 for different times. Black dots correspond to experimental data and the gray lines to the numerical simulations with $h_f=3\times10^{-5}a$.

with $1\leqslant s\leqslant n$. Here, we obtain the power spectrum $|v_s|$ as a function of $\lambda=nP/(s-1)$, where P is the scale of the picture (in units of cm/pixel), since the dominant λ can be related to the average distance between fingers.

By processing the images of the front line for different times as shown in Fig. 12, we obtain the Fourier spectra presented in Fig. 13. For times close to the beginning of the instability [see Fig. 12(a)], one can distinguish two peaks in the spectrum ($t=38.2$ min, lowest gray line in Fig. 13). However, for later times, the shorter-wavelength peak ($\lambda\approx0.55$ cm) grows faster and finally dominates the spectrum. Later, for times greater than 200 min, a secondary peak ap-

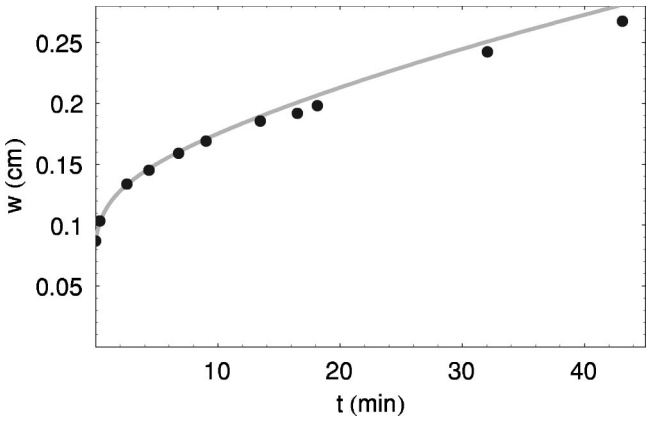

FIG. 11. Comparison of width of the spreading between experiments (black dots) and numerical simulations for $A=3.6\times10^{-4}$ cm^2. The solid and dashed gray lines correspond to $h_f=3\times10^{-5}a$ and $3\times10^{-4}a$, respectively.

pears for even shorter wavelength, $\lambda\approx0.4$ cm.

We note that the details of the emerging patterns vary from experiment to experiment. For example, the experimental results shown in Fig. 12 are characterized by a rather slow evolution of the patterns in the middle of the domain [see Fig. 12(b)]. However, repeating the experiment, using the same glass and the same cleaning procedure, leads to a different pattern distribution. Although the details of the emerging patterns vary, the value of the dominant wavelength is highly reproducible for a given fluid area. We further discuss the aspects of the spectral evolution in Sec. V.

In Fig. 14, we show the width, *w*, of the film along two lines [see arrows in Fig. 12(d)]: One going through the tip of a finger and the other through the central point of an adjacent

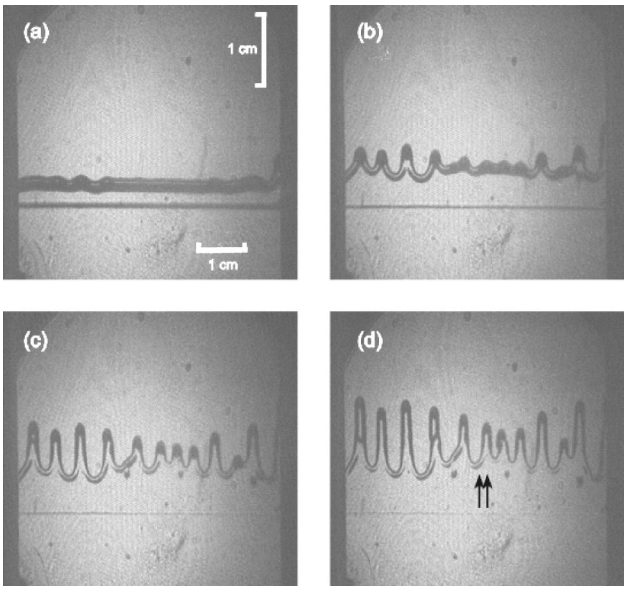

FIG. 12. Evolution of the film using the Schlieren technique for $A=6.75\times10^{-4}$ cm^2 at: (a) $t=38.2$, (b) 101.2, (c) 207.5, and (d) 343.7 min. Arrows point to the *y* coordinates chosen to track the positions of a finger and a trough (see Fig. 14). The white segments stand for the length scale (1 cm) at the substrate.

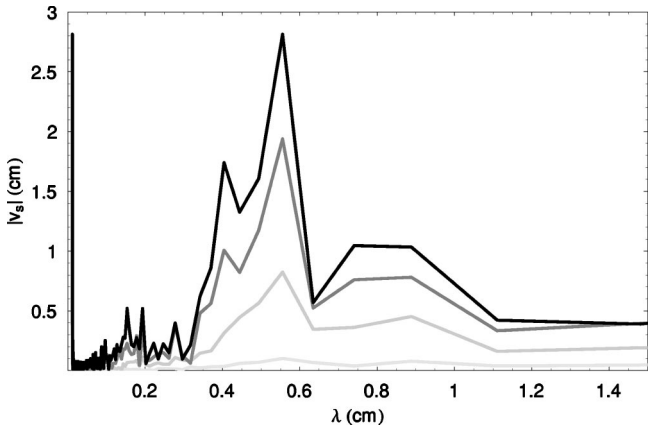

FIG. 13. Fourier spectra of the front lines shown in Fig. 12. Darker lines correspond to later times: $t=38.2$, 101.2, 207.5, and 343.7 min.

trough. For the sake of completeness, we add to the figure the data obtained using the anamorphic system for early times. For comparison, we also plot the trajectory of the unperturbed (straight) front line as given by the numerical simulation (solid line). Figure 14 allows one to estimate a time for the onset of the instability, which is here about $t\approx80$ min. This time is an upper limit, since corrugations might appear for earlier times at different *y* positions.

In Figs. 15–17, we show the corresponding results for the largest area, $A=10.3\times10^{-4}$ cm^2. The Schlieren pictures in Fig. 15 show a very regular pattern of fingers and troughs. This is apparent in the corresponding spectra (Fig. 16), since there is an outstanding peak at $\lambda\approx0.51$ cm from the very early stages of the instability. This suggests that the nonlinear stage of instability development is imprinted by the mechanisms involved in the linear stage. In Fig. 17, we show an expansion of Fig. 8 for later times by including the positions of the fingers and troughs marked with arrows in Fig. 15 from the Schlieren pictures. Just after the onset of the instability, the fingers and troughs clearly depart from the straight front numerical solution (gray line).

The smallest area results ($A=3.6\times10^{-4}$ cm^2), are reported in Figs. 18–20. The spectra have a more complicated struc-

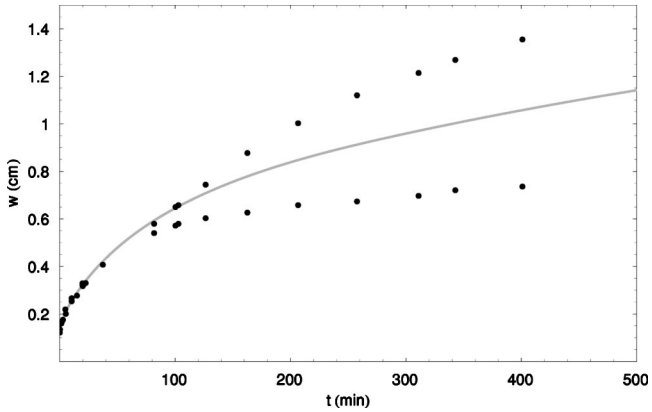

FIG. 14. Positions of a finger and trough (see arrows in Fig. 12) with respect to the rear front from experimental data (dots), and evolution of the unperturbed front line from simulation (solid line), corresponding to the experiment with $A=6.75\times10^{-4}$ cm^2.

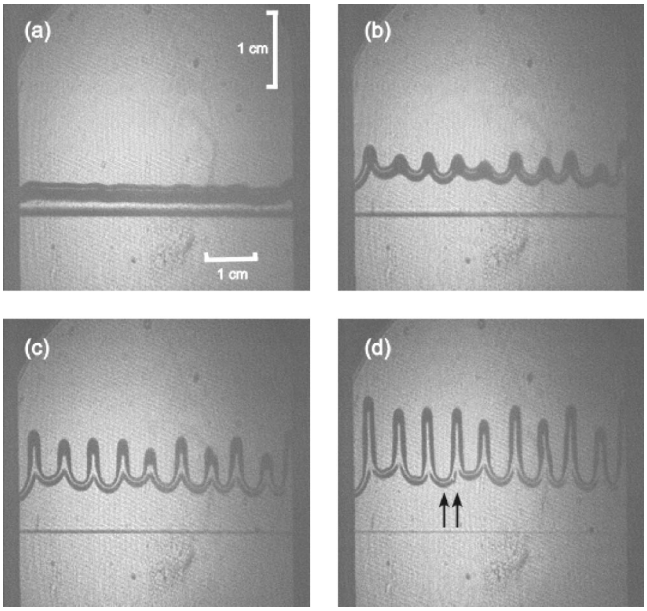

FIG. 15. Evolution of the film using the Schlieren technique for $A=10.3\times10^{-4}$ cm^2 at: (a) $t=17.8$, (b) 54.4, (c) 104.7, and (d) 192.9 min. Arrows point the y coordinates chosen to track the positions of a finger and a trough, see Fig. 17.

ture (see Fig. 19 for early times). For later times, however, there is a well-defined peak (here at $\lambda\approx0.46$ cm), similar to the ones observed in the cases of larger areas. The existence of persistent secondary peaks close to the dominant one is directly related to the shape of the early unstable spectrum ($t=133$ min). The reason why this other peak also grows relatively fast is due to its proximity to the dominant wavelength.

It is interesting to show that the anamorphic technique is also useful in the unstable stage to measure thickness profiles. The measurement must be done along lines where the transverse gradients are negligible, as it occurs along a finger or a trough. In Fig. 21, we show the profile along the symmetry line of a finger from an experiment with area $A=5.5\times10^{-4}$ cm^2. It is obtained by lateral displacements of the

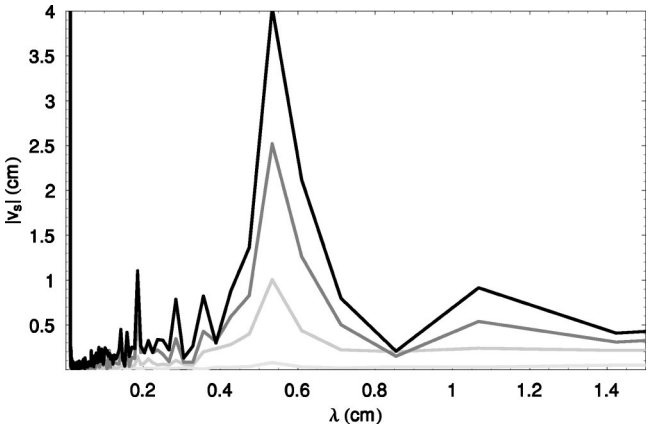

FIG. 16. Fourier spectra of the frontlines shown in Fig. 15. Darker lines correspond to later times: $t=17.8$, 54.4, 104.7, and 192.9 min.

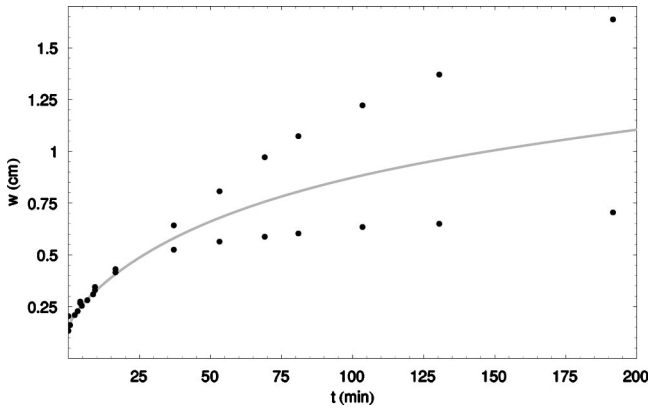

FIG. 17. Positions of a finger and trough (see arrows in Fig. 15) with respect to the rear front from experimental data (dots), and evolution of the unperturbed front line from simulation (solid line), corresponding to the experiment with $A=10.3\times10^{-4}$ cm^2.

glass, so that the light sheet probes the spreading along this line. The frame is moved with a sliding device and the use of a micrometric screw. A similar procedure is followed to obtain the profile along the symmetry line of a trough. To our knowledge these are the first reported simultaneous micrometric profiles of a finger and its adjacent trough for the CV case (on the other hand, the profiles for the CF case of thicker millimetric films are available in literature [8,9,30]). A further analysis of these results and the comparison with numerical simulations is left for a future work.

In summary, the experimental results suggest the existence of stages in the development of the instability. These stages can be defined as follows:

(1) The first stage ($0\leqslant t\leqslant t_0^*$) is characterized by a transient behavior in which the flow evolves from an initial con-

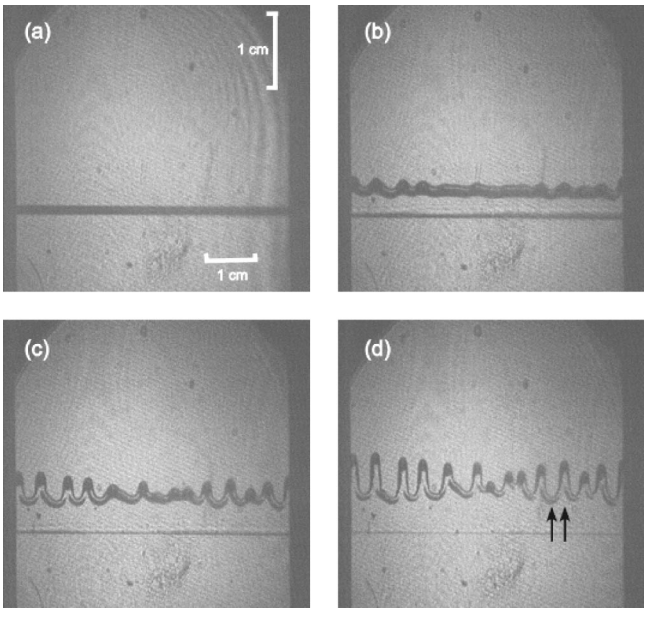

FIG. 18. Evolution of the film using the Schlieren technique for $A=3.6\times10^{-4}$ cm^2 at: (a) $t=0.83$, (b) 133.5, (c) 256.1, and (d) 430.6 min. Arrows point the y coordinates chosen to track the positions of a finger and a trough (see Fig. 20).

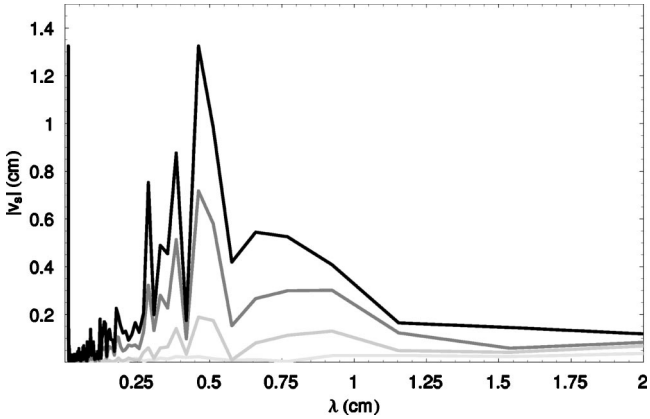

FIG. 19. Fourier spectra of the front lines shown in Fig. 18. Darker lines correspond to later times: $t=0.83$, 133.5, 256.1, and 430.6 min.

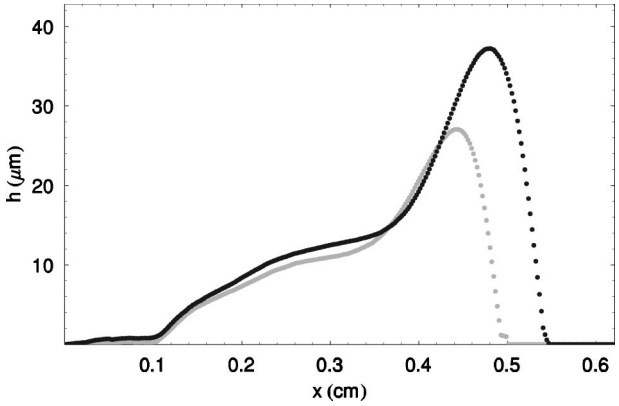

FIG. 21. Thickness profiles along a finger (black dots) and a trough (gray dots) from an experiment with $A=5.5\times10^{-4}$ cm^2 at time $t=52.5$ min.

dition (close to a cylindrical cap) to a structure with a parabolic shape in the rear region and a bump developed in the frontal region. Also, in this stage, the front line is still straight and does not show any appreciable corrugation. A more precise definition of t_0^* will be given below.

(2) Once the bump structure is clearly attained, the small perturbations tend to grow (unstable profile). In other words, the presence of the bump is a key feature for the development of the instability. For this stage, $t>t_0^*$, we develop, in next section, a model for the growth of the amplitude of the perturbations within the linear approximation.

(3) When the amplitude of the perturbations exceeds a certain limit, the nonlinear effects become significant ($t>t_{\mathrm{NL}}$). However, in our experiments, these effects do not change the mean separation between fingers.

We emphasize that for all cross-sectional areas explored here, the instability develops *after* the formation of the bump. In particular, as A is increased, the instability develops faster, but the formation of the bump proceeds on a faster time scale as well. This observation constitutes an important difference with respect to other experiments performed with millimetric (or even thicker) films [1,12]. In those cases, the lubrication approximation is only marginally satisfied, while it is completely fulfilled in our micrometric films. As a consequence, those experiments may have a different sequence of stable and unstable stages. Thicker films often include a rolling motion ("nose") at the advancing front, which stabilizes the flow and is responsible for the initial stable stage [31]. If the film is not too thick, surface tension effects become increasingly important as the fluid thins, and the nose changes its shape to a wedge-shaped profile [32]. Later on, the front region grows a bump and the flow becomes unstable. Instead, in our experiments, there is no rolling stage, but the bump of the front region is present from the very early stages. The instability is not observed at once, but it becomes apparent only after a certain time. We discuss this delay in the next section.

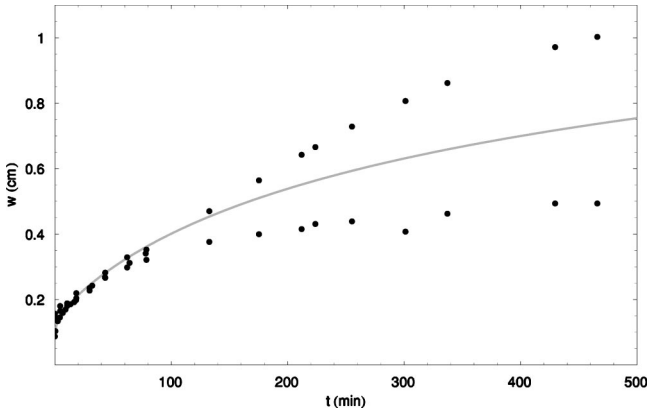

FIG. 20. Positions of a finger and trough (see arrows in Fig. 18) with respect to the rear front from experimental data (dots), and evolution of the unperturbed front line from simulation (solid line), corresponding to an experiment with $A=3.6\times10^{-4}$ cm^2.

V. INSTABILITY ANALYSIS

In this section, we aim to develop a model for predicting the spatial spectrum of the instability, the growth rates of the perturbations and the value of the dominant wavelength λ_m. At present, there is no thorough analysis of the contact line instability for the CV problem. Instead, a fair amount of literature is devoted to the linear stability analysis of the CF problem. Here, we apply the results of the CF case to produce a predictive model for the CV configuration.

A. Constant flux revisited

Thanks to the translational invariance in the CF case, the solution of the y-independent version of Eq. (1) is of the traveling wave type. Thus, for a constant thickness, h_p, in the far region behind the front (plateau), we have a dimensionless solution of the form,

$$h = h_p H(\xi), \qquad \xi = (x - ut)/\ell, \tag{6}$$

where

$$\ell = (a^2 h_p)^{1/3}, \qquad u = u_0(1 + b + b^2), \tag{7}$$

with $u_0=\rho g h_p^2/3\mu$ and $b=h_f/h_p$. The main feature of this solution is the presence of the bump in the front region

TABLE I. Maximum growth rates and critical wavelengths for several b's.

$b=h_f/h_p$	$\sigma_{\max}\ell/u_0$	$\lambda_{\max}/\ell$	λ^*/ℓ
10^{-1}	0.127	12.84	8.33
10^{-2}	0.285	12.58	7.42
5×10^{-3}	0.340	12.57	7.34
3×10^{-3}	0.377	12.56	7.23

[2,19]. As it is well known in literature, this bump is the signature indicating the instability of the solution. In the linear stability analysis of this problem, it is assumed that there is a transverse perturbation of the base solution $H(\xi)$ characterized by a wavelength λ. Thus, the perturbed solution expanded in normal modes is written as

$$\mathcal{H}(\xi,y,t) = H(\xi) + \epsilon g(\xi)\cos(ky)\exp(\sigma t), \tag{8}$$

where ϵ is the (small) amplitude of the perturbation, $g(\xi)$ is the eigenfunction, σ is the growth rate (eigenvalue), and $k=2\pi/\lambda$.

Upon substitution of Eq. (8) into Eq. (1), we keep terms only up to $O(\epsilon)$. The terms of $O(\epsilon^0)$ yield an ordinary differential equation [2], whose solution is $H(\xi)$. The terms of $O(\epsilon)$ constitute an eigenvalue problem of the form $\mathcal{L}g(\xi)=\sigma g(\xi)$, where $\mathcal{L}$ is a linear operator, whose coefficients depend on the base solution $H(\xi)$ [33]. We solve this problem and obtain σ as the maximum value of the discretized spectrum. These calculations are performed for k's in the range $0\leqslant k\leqslant 1.2$.

For a given b, there are two relevant wave numbers: (a) k_{max} for which $\sigma(k_{max})$ is the maximum, σ_{max}, and (b) $k^*=2\pi/\lambda^*$, which yields $\sigma(k^*)=0$ (marginal stability), such that the solution is unstable for $k<k^*$ $(\lambda>\lambda^*)$, and stable otherwise. Calculated values of these parameters are reported in Table I for some values of b. Clearly, $\sigma_{\max}$ shows a stronger dependency on b than the wavelengths λ^* and $\lambda_{\max}$.

Interestingly enough, when all the growth rates $\sigma(k)$ for various b's are plotted in the normalized form

$$\frac{\sigma}{\sigma_{\max}} = F(q), \tag{9}$$

where $q=k/k^*=\lambda^*/\lambda$, they nearly collapse onto a single curve (see Fig. 22). For the purpose of analyzing the CV case, we look for a simple analytical form that would represent well all these eigenvalues, in particular in the unstable range. It turns out that the polynomial fit that one may expect based on the small q limit of the linear stability analysis [15] (expansion in even powers of q) is not appropriate for the whole q range. A better approximation is obtained by using a general functional form $q^2(1-q^p)$ where p is a rational number. We find best agreement by using

$$F(q) = 95q^2(1-q^{1/17}), \tag{10}$$

which is also plotted in Fig. 22. This fit is used in the next section, and it implies that $\lambda^*\approx 0.61\lambda_{\max}$. The departures from this function increases for $q>1$, but the fitting in the unstable range is reasonably good, and it will be helpful in the model for CV case developed in the following section.

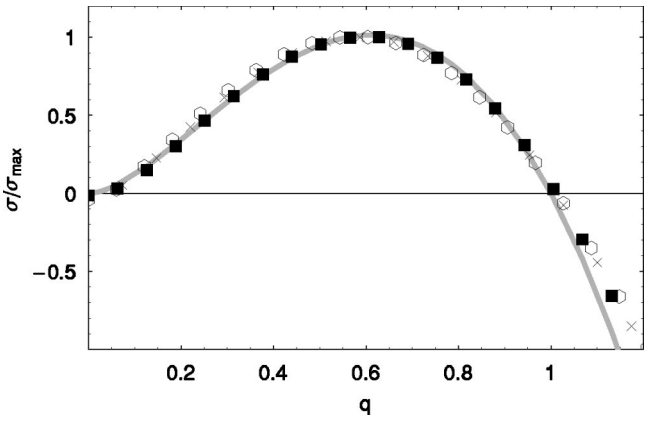

FIG. 22. Eigenvalues of the dispersion relation for the CF case for $b=0.01$ (crosses), 0.005 (squares), and 0.003 (open pentagons). The solid line is a fitting curve, specified by Eq. (10).

B. Constant volume configuration: Adiabatic model

A major hindrance to performing the linear stability analysis of the unperturbed solution $h(x,t)$ for the CV case, is the fact that the base solution is time dependent, as outlined above. Here, we extend the linear stability analysis of the CF case by assuming that the base profile evolves sufficiently slowly relative to the growth rate of the perturbations (adiabatic approach).

Let us consider a profile $h(x,t_0)$ after the fluid starts spreading, with $t_0\geqslant t_0^*$. Since at $t=t_0$, the flow has already developed a bump–plateau structure, we perform the analysis by perturbing the flow by a transverse corrugation characterized by a wavelength λ and an initial amplitude $I_0=I(t_0)$. A key point in describing the linear evolution of the instability is to assume that the unperturbed state changes so slowly during this stage that the perturbation evolves on top of a quasi-steady base flow. Thus, the asymptotic growth rates of the CF case can be considered as the instantaneous growth rates of the CV case. This assumption requires that the amplitude of the perturbation be small enough, so not to modify significantly the base flow (linear regime). Therefore, every component of the spatial Fourier spectrum of the perturbation evolves independently from one another.

We attempt to approximate the bump region of the CV flow by the corresponding profile in the CF case for the same h_f. The idea underlined in this approximation is that the instability basically depends on the thickness structure of this region, while the flow far behind does not affect the behavior of the front. In the CF case, the characteristic time and length scales as $\ell/u_0\approx h_p^{-5/3}$ and $h_p^{1/3}$, respectively [see Eq. (7)]. Thus, the *instantaneous* growth rate in the CV case becomes [see also Eq. (9) and [33]]:

$$\sigma(q) = \sigma_{\max} h_p^{5/3} F(q) \tag{11}$$

where

$$q = \frac{\lambda^*}{\lambda} h_p^{1/3}(t). \tag{12}$$

Here, $h_p(t)$, λ are expressed in units of the capillary length a, and t, σ are in units of

$$\tau = 3\mu a/\gamma, \tag{13}$$

and τ^{-1}, respectively. In order to avoid cumbersome notation, we use the symbols of the previous section to denote the present dimensionless variables. The values of $\sigma_{\max}$ and λ^* expressed in these units are given in Table I.

In a typical experiment, the range of $b(t)=h_p(t)/h_f$ is between 10^{-3} and 5×10^{-3}. As shown in Fig. 22 and Table I, there are no significant variations of $\sigma_{\max}$, λ^* and the shape of function F within this range.

The instantaneous growth rate satisfies $\sigma=I^{-1}dI/dt$, so we have

$$I(\lambda,t) = I_0(\lambda)\exp\left(\int_{t_0}^{t} \sigma(q(t'))dt'\right). \tag{14}$$

Thus, Eqs. (11) and (12) allow us to calculate the instantaneous growth rate of the perturbation as a function of the dimensionless thickness $h_p(t)$, and Eq. (14) predicts its amplitude.

The experimental results show that for a given time there exists at least one dominant wavelength, where the spectra have a peak. In order to obtain an estimate of this wavelength, we assume here that the initial amplitude I_0 =constant is the same for every λ, thus yielding a single maximum of the amplitude $I_{\max}$ at $\lambda=\lambda_{\max}$. Then, from Eq. (14), we have the condition

$$\int_{t_0}^{t} \left.\frac{\partial\sigma(q)}{\partial\lambda}\right|_{\lambda=\lambda_{\max}} dt' = 0, \tag{15}$$

which, for given values of t_0 and t, allows one to calculate $\lambda_{\max}$.

To proceed, we must define an appropriate way of determining the parameter $h_p(t)$. For this purpose, let us consider a CF flow with a certain value h_p of the (asymptotic) flat region, such that it has a bump height h_b coincident with the one of the CV case with the same h_f. The idea is to approximate the CV flow by the solution of a CF case which fits the bump region the best. Note that this model is intended to describe only the instability of the contact line and not the complete flow in the CV problem. The underlined concept is that the instability basically depends on h_b and the slope at the contact line, and that other details of the flow are not so relevant.

In order to ensure that the model is used within the adiabatic and linear approximation, the time t_0 must be in the interval $t_0^* \leqslant t_0 \leqslant t_{NL}$ (see also the end of Sec. IV B). The adiabatic condition requires that the relative rate of variation of h_p,

$$\beta = \frac{1}{h_p}\frac{\partial h_p}{\partial t}, \tag{16}$$

must be smaller than the instantaneous growth rate of the perturbation. If this condition is fulfilled for the growth rate of the dominant wavelength $\lambda_{\max}$, then it is satisfied for all other λ's. We can obtain the lower bound t_0^* as the time at which $\beta(t_0^*)=\sigma(t_0^*)$ for $\lambda_{\max}$. For this purpose, we assume a guess value of t_0 and use Eq. (15) to find $\lambda_{\max}$ by integrating from t_0 to a sufficiently large time t. If $\sigma(\lambda_{\max})$ as given by Eq. (11) is less than β at t_0, we choose a smaller value of t_0; otherwise, t_0 must be increased. This iteration scheme yields t_0^*, i.e., the lower bound of t_0. This procedure is accurate since $\lambda_{\max}$ depends only weakly on t_0 for very large t.

The experiments show that the instability actually occurs for t_0's greater than t_0^*, so that the requirement of slow change of the base state is fully satisfied. Thus, the predicted spectra results presented below use the value of t_0 as obtained from the experiments.

Figure 23 shows both the experimental spectra and the model results at four different times presented in Fig. 12. The model predictions are based on the linear evolution of the experimental spectrum $I_0(\lambda)$ from the earliest time t_0 =38.2 min (lower gray line). Figures 23(a) and 23(b) that concentrate on early times, show that close to the dominant wavelength $\lambda=\lambda_{\max}\approx0.55$ cm, there is a very good agreement between the model and the experiments.

Figure 23 also presents the spectra (dotted lines) obtained assuming constant initial amplitude, I_0. This constant is chosen as the experimental maximum at t_0, and therefore the dotted lines provide an envelope for the model results that use the details of experimental configuration at time t_0. These envelopes will help us understand some features of the results that we discuss next.

One of these features is another peak at $\lambda\approx0.9$ cm. For this peak, the model predicts the growth that is slower corresponding to the experimental one. The discrepancy can be understood by observing the slope of the envelope shown in Fig. 23. In the zones where the slope of this envelope is very large, an error in λ plays a significant role in the determination of the corresponding growth rates. In fact, the discrete character of the DFT spectrum leads to an error in the determination of λ of the order [see text after Eq. (5)] $\Delta\lambda=\lambda/(s-1)=\lambda^2/nP$ (≈0.15 cm for $\lambda=0.9$ cm). Thus, for larger λ, there is a larger error in its determination.

Since for $\lambda\approx0.9$ cm there is a significant change in the slope of the envelope within $\Delta\lambda$, the growth rate predicted by the model may differ significantly from that given by the DFT. Note also that based on these arguments, the model is expected to be more accurate for wavelengths close to the dominant one.

Figures 23(c) and 23(d) show the results for later times. Although we observe an increasing departure of the growth rates from the linear model, the dominant wavelength given by the model is still close to the experimental one. One can expect that nonlinear effects account for this difference, since the shape of the contact line corresponding to these later times [see Figs. 12(c) and 12(d)] has the characteristic features of the nonlinear stage of the instability (e.g., the length

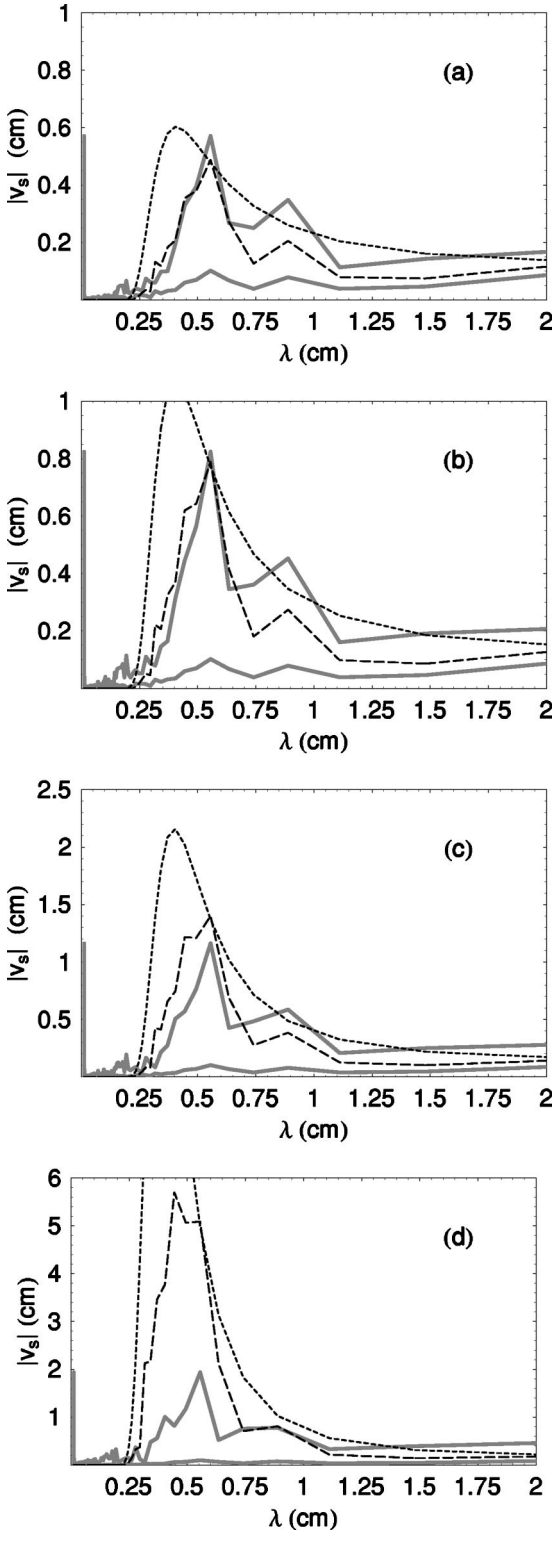

FIG. 23. Spectral evolution of the front line for $A=6.75\times10^{-4}$ cm^2 (see Fig. 12). (a) The lower and upper gray lines correspond to the experimental spectra at $t_0=38.2$ min and $t=82.8$ min. respectively. The dashed black line is the spectrum predicted by the model at t assuming a linear evolution from the spectrum at t_0. The dotted line is the spectrum obtained evolving the model from the uniform spectrum at $I_0=$constant at t_0. (b), (c), (d): The same as (a) for final times $t=101.2$, 127.3, and 207.5 min, respectively.

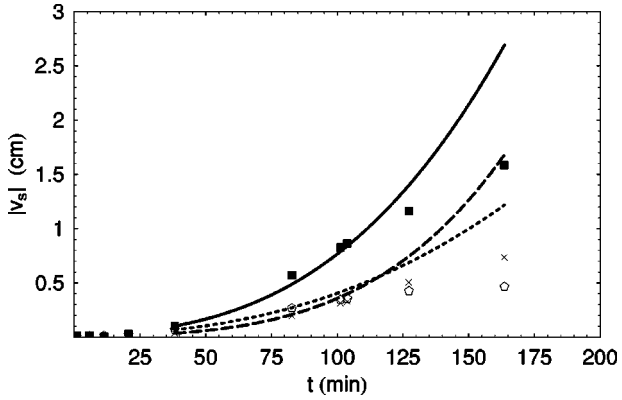

FIG. 24. Time evolution of the modal amplitudes for $A=6.75\times10^{-4}$ cm^2. The symbols correspond to experimental data and the lines to the model results for $\lambda_{max}=0.55$ cm (squares, solid line), $\lambda=0.63$ cm (pentagons, dotted line), and $\lambda=0.41$ cm (crosses, dashed line).

of fingers is much larger than their separation). Another signature of nonlinear effects can be traced to the increased amplitudes of short wavelengths for late times. To see this, note that the experimental spectra in Fig. 13 show that the amplitudes for $\lambda<\lambda^*$ are not as small as one would expect based on the linear stability analysis. Our interpretation is that part of the energy of the linear modes is transferred by nonlinear processes to shorter wavelengths (energy cascade). Essentially, what occurs here is that the fingers' shape change for later times, becoming more pointing with parallel sides. A description of these features then requires shorter wavelengths. This mechanism subtracts energy from the dominant wavelengths and it may then be another source of the difference between the experimental results and the linear model for late times. Similar features can be also observed for different fluid areas, shown in Figs. 16 and 19.

An additional effect that must be taken into account to better understand the instability for late times is the increase of the ratio $b=h_f/h_p$, due to the fact for fixed h_f, h_p decreases. This increase of b leads to the decrease of the maximum growth rate, as shown in Table I. This effect only plays a minor role when the model is applied to the linear stage, in which b is of the order of 10^{-3}. However, for the advanced nonlinear stages, b is significantly larger. As a consequence, the growth rates predicted by the model that uses a constant value of σ_{max} in Eq. (11) corresponding to small b, are certainly greater than those of the actual flow for later nonlinear stages where b is not so small.

For very long wavelengths ($\lambda>2$ cm), the experimental spectra have relatively high amplitudes. These wavelengths may be affected by the boundaries, due to the finite extension (in the y direction) of the film. Nevertheless, these effects do not influence the behavior of the dominant wavelength, since λ_{max} is much smaller than the lateral width of the experimental domain.

Figure 24 presents another test of the model. This figure compares the model predictions for the time evolution of modal amplitudes extracted from the experimental spectra shown in Fig. 12. For brevity, we have chosen the amplitudes of the dominant wavelength, λ_{max}, and of two other λ's (a

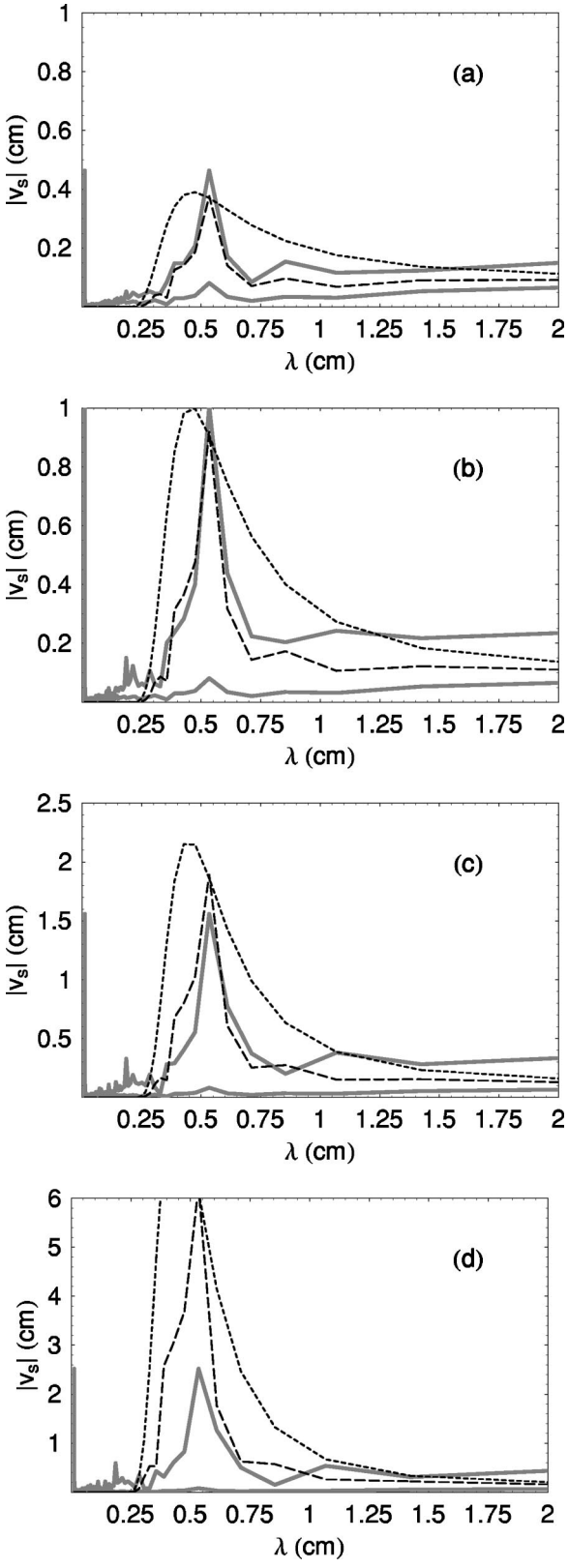

FIG. 25. Spectral evolution of the front line for $A=10.3\times10^{-4}$ cm^2 (see Fig. 15) at final times $t=17.8$, 54.4, 70.4, and 104.7 min in (a)–(d), respectively (here $t_0=17.8$ min). See the legend of Fig. 23 for additional information.

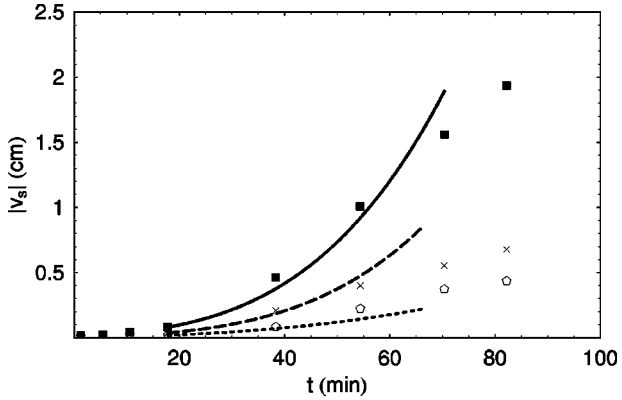

FIG. 26. Time evolution of the modal amplitudes for $A=10.3\times10^{-4}$ cm^2. The symbols correspond to experimental data and the lines to the model results for $\lambda_{max}=0.53$ cm (squares, solid line), $\lambda=0.71$ cm (pentagons, dotted line), and $\lambda=0.47$ cm (crosses, dashed line).

shorter one and a longer one). For early times, the agreement between the model and the experiment is very good. For late times, which start close to $t=120$ min, there is an increasing departure from the linear model predictions.

Figure 25 shows the spectra for the large area case $A=10.3\times10^{-4}$ cm^2 [see Fig. 15(a)]. Here, we observe many similarities but also some differences compared to the previous case. Regarding similarities, there is good agreement between the model and the experiment for the emerging dominant wavelength, as well as for the amplitudes at early times. This agreement is confirmed by the time evolution of modal amplitudes shown in Fig. 26. In this figure, we see that the transition to the nonlinear regime occurs for times close to $t=50$ min. The main difference between these spectra and the previous ones is the appearance of a strong dominant wavelength with very weak side peaks. This feature can be qualitatively understood by visual comparison of Figs. 12 and 15—the patterns shown in Fig. 15 are much more regular, leading to better defined dominant wavelength.

Next, Fig. 27 shows the results for smaller fluid area, $A=3.6\times10^{-4}$ cm^2. The spectra still have a dominant wavelength, but the amplitudes of the side peaks are now closer to that of the main peak. In spite of this more complex structure, the model still accurately predicts the value of the dominant wavelength. The time evolution of modal amplitudes, shown in Fig. 28 is again in good agreement with the model for early times. The transition time towards the nonlinear regime is now close to $t=180$ min. Regarding differences to the cases of larger areas, we note that the envelope here is flatter, and so the maximum growth rate is closer to the ones of the neighboring modes. As a consequence, the development of a clearly dominant wavelength is slower compared to the larger areas.

Before concluding this section, we briefly discuss an alternative approach to the analysis of the experimental data, with the main goal of verifying that our results are not affected by possible spatial nonuniformities of the substrate. Therefore, we complement our (global) Fourier analysis by a local wave number study using the *complex demodulation* of the shape of the corrugated contact line. This procedure may

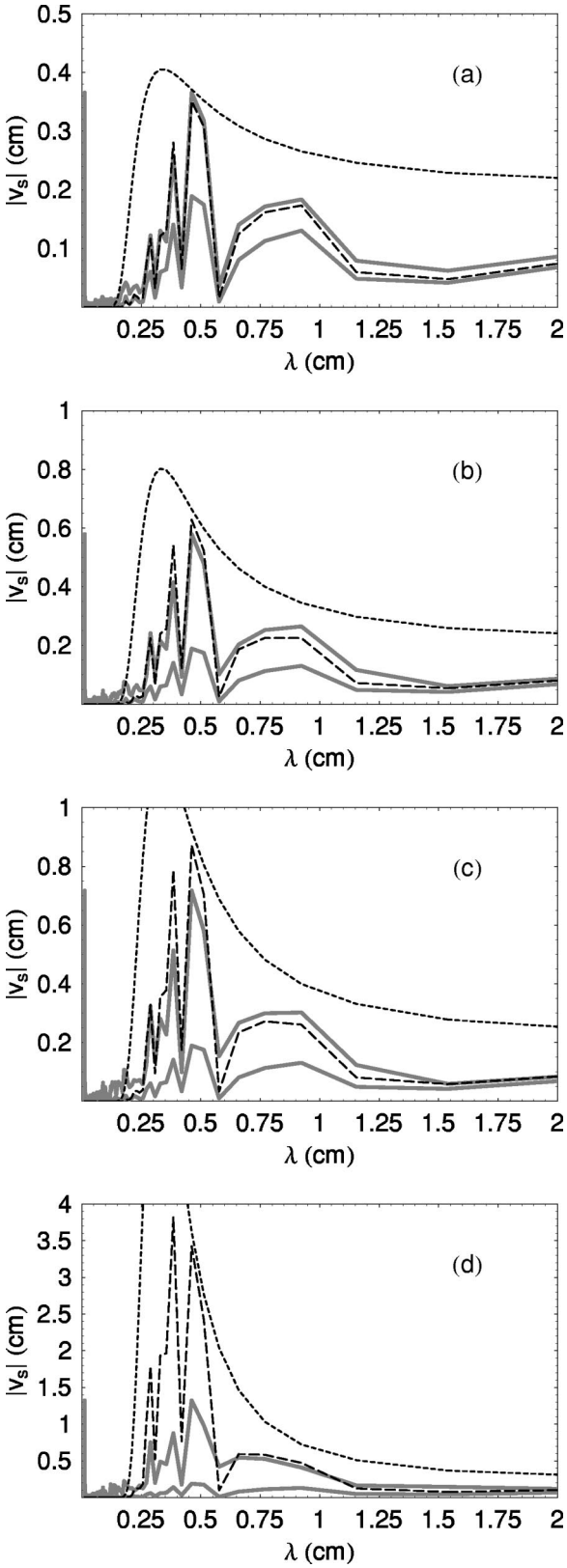

FIG. 27. Spectral evolution of the front line for $A=3.6\times10^{-4}$ cm^2 (see Fig. 18) at final times $t=176.2$, $t=224.6$, 256.1, and 430.6 min in (a)–(d), respectively (here $t_0=133.5$ min). See the legend of Fig. 23 for additional information.

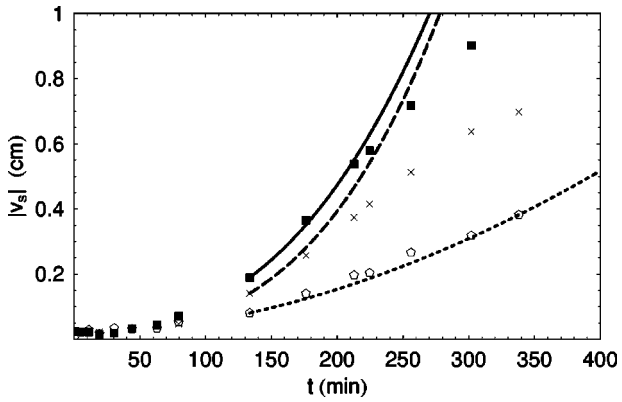

FIG. 28. Time evolution of the modal amplitudes for $A=3.6\times10^{-4}$ cm^2. The symbols correspond to experimental data and the lines to the model results for $\lambda_{max}=0.46$ cm (squares, solid line), $\lambda=0.66$ cm (pentagons, dotted line), and $\lambda=0.38$ cm (crosses, dashed line).

be regarded as a local version of the previously presented Fourier analysis, and it consists of demodulation of the digitized spreading width $w(y,t)$ [see Eq. (4)] obtained from the Schlieren pictures. By defining the wave number $k_0=2\pi/\lambda_0$, we write the demodulated function as [34]:

$$W(y,t)=[w(y,t)-w_{\mathrm{av}}(t)]e^{-ik_0y} \tag{17}$$

where $w_{\mathrm{av}}(t)$ is the width averaged along the transverse y direction. Here, we take λ_0 equal to the dominant wavelength λ_{max} as given by the Fourier analysis. Thus, we assume that the contact line can be described by a monochromatic signal with slowly varying both amplitude $R(y,t)$ and phase for a given time t. We extract an approximation to $R(y,t)$ by employing a least-squares filter as described in Ref. [34]. Since we want to compare this amplitude with the one given by Fourier analysis, $|v_s|$ [see Eq. (5)], we define $R_n=\sqrt{n}R(y,t)$.

Figures 29(a)–29(c) shows the results of this technique applied to the linear stage of the experimental data presented earlier in increasing order of the area A. In Fig. 29(a), we show the time evolution of R_n at three fixed transverse positions along the spreading front, located approximately $1/4$ (dotted-dashed line), $1/2$ (dotted line), and $3/4$ (dashed line) along the spreading in the y direction, measured from the left edge. Note that even if the local amplitudes are different, the curves are almost parallel to each other, thus indicating that the growth rate $d\log R_n/dt$ of the demodulated amplitude is almost the same at all locations. Therefore, we do not find any evidence of spatial nonuniformity of the substrate. For comparison, we also show [solid line in Fig. 29(a)] the amplitude $|v_s|$ of the dominant mode λ_{max} as given by the model. Clearly, the model describes well the growth rates obtained by using complex demodulation technique.

In Figs. 29(b) and 29(c), we present the results for larger areas, corresponding to Figs. 12 and 15. These figures also lead to the same conclusion regarding spatial uniformity of the substrate, and the agreement of the global Fourier analysis with the complex demodulation technique. We note that the first point in the curve at $1/4$ (dotted-dashed line) in Fig. 29(c) is not completely reliable since the difference $w-w_{\mathrm{av}}$ is

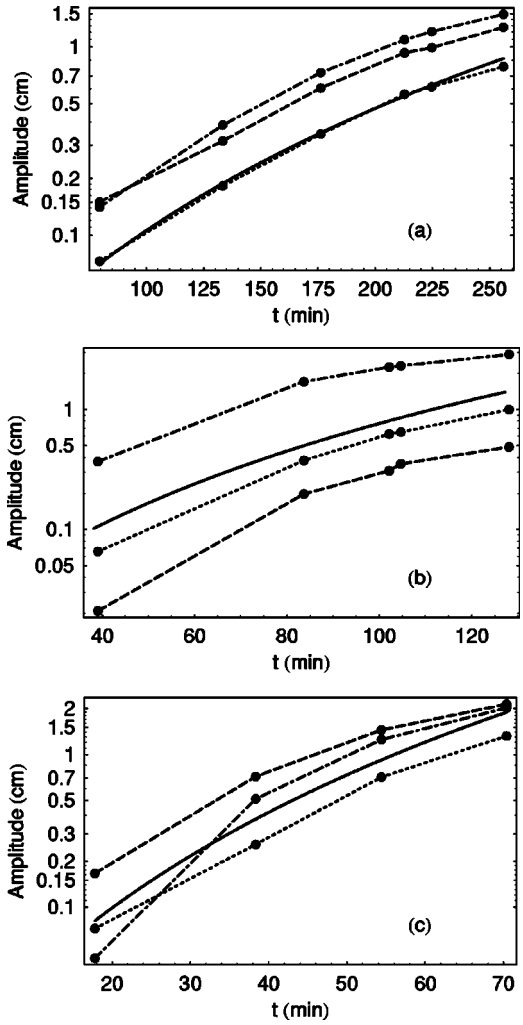

FIG. 29. Time evolution of the amplitude R_n of the complex demodulated contact line at $\lambda_0=\lambda_{max}$ for: (a) $A=3.6\times10^{-4}$, (b) 6.75×10^{-4}, and (c) 10.3×10^{-4} cm^2. The dotted–dashed, dotted, and dashed lines correspond to 1/4, 1/2, and 3/4 of the distance along the spreading in the y direction, respectively. The solid line corresponds to the amplitude $|v_s|$ of the dominant mode λ_{max} as given by the model.

very small there [see Fig. 15(a)], and then the demodulation technique, including the filtering process, yields a large relative error.

C. Other approaches to h_p

The fitting process of the bump height explained above yields values of h_p that are generally higher than those of the actual plateau zone (mentioned in Sec. III A) connecting the bulk and bump regions. One might question whether a model that adjusts h_p to the actual plateau thickness could lead to better results. In this alternative approach, the function $h_p(t)$ can be obtained from the numerical simulation by defining it as the thickness of the second inflection point behind the bump. This choice is convenient because it allows for a simple tracking of the point, and it corresponds to the plateaulike zone which connects the rear parabolic and frontal bump region.

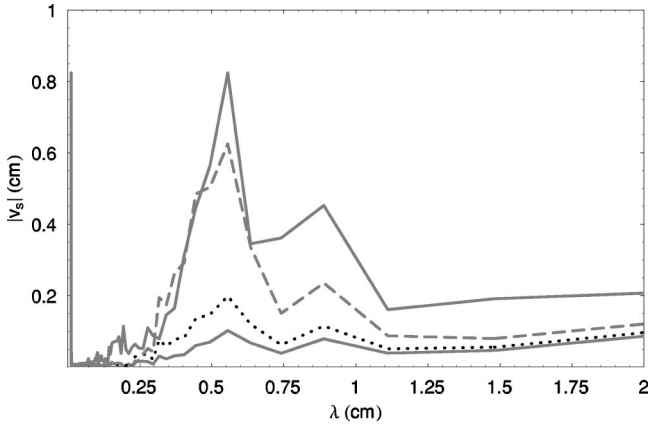

FIG. 30. Comparison of experimental results for the case shown in Fig. 23(a) with the spectral evolution of the front line using: Plateau adjustment of h_p (dotted line), and adjustment by using Huppert's solution ($h_p=h_H$, dashed line).

Figure 30 shows the results obtained using this approach applied to the experiment performed using $A=6.75\times10^{-4}$ cm^2. The comparison of the dotted line obtained using this fit and of the experimental curve demonstrates that this fitting mechanism fails to describe the experimental results [viz. Fig. 23(a) for the results obtained using bump-fitting approach]. Similar results hold for all other explored cross-sectional areas, reinforcing the argument that the instability development in the linear regime is governed by the bump and front region while the rear zone plays only a minor role.

Another option is to approximate $h_p(t)$ by the value given by Huppert's formula [1]. This analytical solution is obtained by neglecting surface tension effects, and thus it does not predict the bump region (see the Appendix). However, it is expected to be a good approximation of the rear zone for large times. Therefore, one hopes that it should be possible to use $h_p(t)\approx h_H(t)$ [see Eq. (A3)]. The computed results using this model are also plotted in Fig. 30 (dashed line). We see that this approach still underestimates the growth rate of the linear stage of the instability.

There are several additional drawbacks regarding the use of Huppert's solution to estimate h_p for $t\geqslant t_0$. For the times when the linear model is expected to hold, neither the thickness profile nor the position of the contact line is correctly predicted by this analytical solution. This is illustrated in Fig. 31. This figure shows that Eq. (A2) [solid line in Fig. 31(a)] predicts much too fast spreading of the film, compared to the experimental results (dots) [the time in Eq. (A2) has been shifted in order to get the right value of $w(t=0)$]. The portion of the fluid area that should be placed in the bump is relocated in the bulk, thus leading to an overestimate of the width. Furthermore, the profiles for the early stages of the instability (see, e.g., Fig. 21) are also poorly described by Huppert's solution.

In spite of the failure of this solution to describe the stable stage as well as the early stages of the instability, one may wonder why the departure of the predicted growth rates from the experimental data (see Fig. 30) is only about 20%. This fact can be explained by a mechanism of cancellation of

errors. Note that h_p (as given by h_H) is initially too large (it diverges as $t \to 0$), and it also decreases too fast [see Eq. (A3)]. As a consequence, for times close to t_0, this approach leads to a perturbation's growth that is faster than expected [see Eq. (11)]. However, this approach also diminishes the growth rate too strongly for later times. Upon time integration, these two departures from the actual behavior almost compensate for each other, and the results for the amplitude of the perturbation are then masked by this cancellation. For even later times, one could hope that, due to the asymptotic character of Huppert's solution, it could be appropriate to describe the unperturbed y-independent flow for larger times, However, for those times, the perturbations have grown enough to invalidate the modeling of the growth rates by a linear approach, no matter how we define h_p.

VI. SUMMARY AND CONCLUSIONS

In this work, we report detailed experimental results of the spreading of a constant volume of PDMS oil down a vertical glass substrate. We study this problem by combining experimental and theoretical/computational techniques. The experiments employ two optical techniques: One requires the use of an anamorphic lens, and the other is based on the Schlieren method. The analysis is performed by comparing the experimental data with numerical simulations and by developing analytical models.

The anamorphic lens technique allows one to measure the thickness profile and the width of the film. It is mainly used in the stable stage of the experiments before the onset of the instability. From the measured profiles we obtain the cross-sectional area of the uniform fluid strip. Since the area is accurately measured, we are in a position to very precisely determine the thickness of the precursor film which numerically reproduces the evolution of the experimental profiles of an arbitrary single experiment. The outcome of this procedure is the thickness of 43 nm which is a value in agreement with those reported and estimated in literature. This value is directly used as an input to numerical simulations that use different fluid cross-sectional areas. The calculated profiles are in very good agreement with the experimental data obtained using these different areas.

The images obtained using the Schlieren technique are used to study the shape of the front line after the onset of instability. Here, we perform a discrete Fourier transform of the fluid front lines. The resulting spatial spectra show a dominant wavelength which is determined during the linear stage of the instability development. The experiments show that this wavelength is a decreasing function of the area A. Also, the reported experimental results allow one to determine the average growth rate for all spatial modes occurring in the experiment by comparing two spectra at successive times.

We developed a linear model to account for the time evolution of the amplitude of each mode. It uses the growth rates of the instability of a CF problem properly scaled to consider the thinning of the average thickness in the CV case. A key point in the model is the determination of the appropriate value of the plateau thickness to be used in the CF solution.

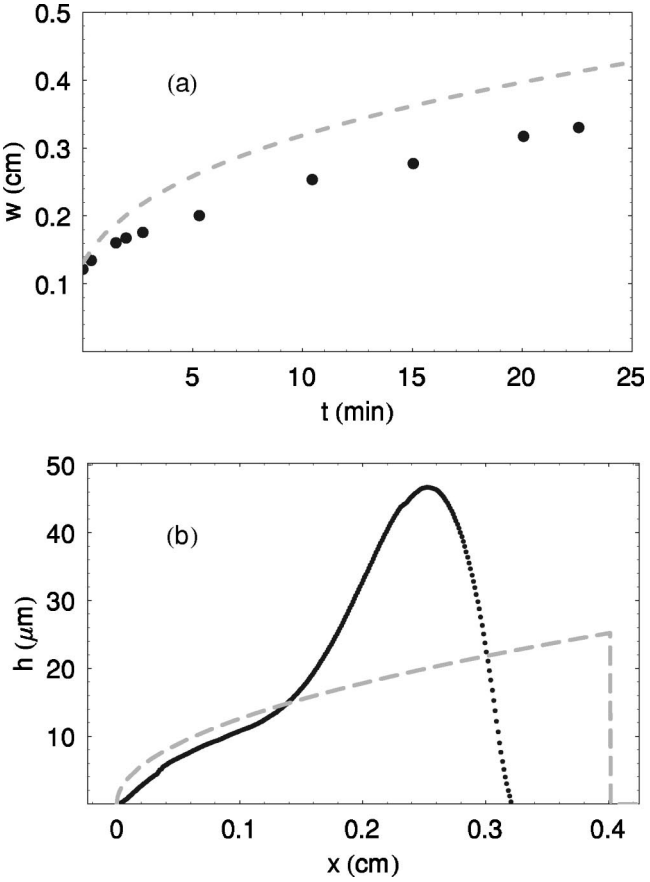

FIG. 31. Comparison of Huppert's solution (gray dashed lines) with the experiment of $A = 6.75 \times 10^{-4}$ cm^2 (black dots). (a) Width of the spreading. (b) Thickness profile for $t = 20.07$ min. See also Figs. 4(c) and 5.

Several possibilities are considered, and we show that the best fit to the experimental results is obtained by choosing such a value that the bump heights of these two problems (CV and CF) agree. In particular, we show that the use of the Huppert's solution fails to produce quantitatively correct results for both stable and unstable stages of the flow.

In summary, our experimental techniques allow one to provide a detailed quantitative description of several features of the problem not previously reported in literature. The accurate determination of the relevant parameters of the experiments (such as the thickness of the precursor film, cross areas, thickness profiles, spatial spectra of the modes, and growth rates) are essential to test the validity of the approximations involved in the lubrication theory and the contact line physics.

ACKNOWLEDGMENTS

Four of the authors (A.G.G., J.D., J.G., and R.G.) acknowledge support from Consejo Nacional de Investigaciones Científicas y Técnicas (CONICET-Argentina), and another author (L.K.) support from NSF Grant No. INT-0122911.

APPENDIX: HUPPERT'S SOLUTION

If we ignore the y dependence of the flow, we are left with a one-dimensional problem. For late times, when the transient effects associated with the initial release of the fluid have decreased enough, a self-similar solution, that balances the weight of the fluid and the viscous force on the plane [i.e., the first and third terms in Eq. (1)], can be obtained. Thus, by neglecting surface tension, one reaches the solution (first derived by Huppert [1]) of the form

$$h(x,t) = \left(\frac{x}{3t}\right)^{1/2}, \tag{A1}$$

where h, x are in units of a, and t is in units of τ (see Sec. V B). The domain of the solution ends abruptly at

$$x_H(t) = \left(\frac{27}{4}A^2 t\right)^{1/3}, \tag{A2}$$

where the thickness is

$$h(x_H) = h_H = (A/2t)^{1/3}. \tag{A3}$$

By replacing this solution in the neglected terms, we find that it holds for (see [35]) $1 \ll (48x^5 t)^{1/2}$. Thus, Huppert's self-similar solution is reached asymptotically as $t \to \infty$. However, as noted by Hocking [35], the main criticisms that can be made to this solution regard the validity of the lubrication approximation. It violates the small slope hypothesis both at the leading edge, where h goes abruptly from h_H to (practically) zero, and at the rear wall, where the slope is infinite. Note that the inclusion of surface tension, i.e., the fourth-order term in Eq. (1) breaks self-similarity.

[1] H. Huppert, Nature (London) **300**, 427 (1982).
[2] A. L. Bertozzi and M. P. Brenner, Phys. Fluids **9**, 530 (1997).
[3] N. Fraysse and C. M. Homsy, Phys. Fluids **6**, 1491 (1994).
[4] F. Melo, J. F. Joanny, and S. Fauve, Phys. Rev. Lett. **63**, 1958 (1989).
[5] A. M. Cazabat, F. Heslot, S. M. Troian, and P. Carles, Nature (London) **346**, 824 (1990).
[6] M. J. Tan, S. C. Bankoff, and S. H. Davis Phys. Fluids A **2**, 313 (1990).
[7] X. Fanton, A. M. Cazabat, and D. Quéré, Langmuir **12**, 5875 (1996).
[8] M. F. G. Johnson, Ph.D. thesis, Northwestern University, 1997.
[9] M. F. C. Johnson, R. A. Schluter, and S. C. Bankoff, Rev. Sci. Instrum. **68**, 4097 (1997).
[10] J. R. de Bruyn, Phys. Rev. A **46**, R4500 (1992).
[11] J. M. Jerrett and J. R. de Bruyn, Phys. Fluids A **4**, 234 (1992).
[12] H.-C. C. I. Veretennikov and A. Indeikina, J. Fluid Mech. **373**, 81 (1998).
[13] F. Heslot, A. M. Cazabat, and P. Levinson, Phys. Rev. Lett. **62**, 1286 (1989).
[14] H. P. Greenspan, J. Fluid Mech. **84**, 125 (1978).
[15] S. M. Troian, E. Herbolzheimer, S. A. Safran, and J. F. Joanny, Europhys. Lett. **10**, 25 (1989).
[16] M. A. Spaid and G. M. Homsy, J. Non-Newtonian Fluid Mech. **55**, 249 (1994).
[17] E. B. Dussan V., J. Fluid Mech. **77**, 665 (1976).
[18] L. M. Hocking and A. D. Rivers, J. Fluid Mech. **121**, 425 (1982).
[19] J. Diez, L. Kondic, and A. L. Bertozzi, Phys. Rev. E **63**, 011208 (2001).
[20] J. Diez and L. Kondic, J. Comput. Phys. **183**, 274 (2002).
[21] J. Diez and L. Kondic, Phys. Rev. Lett. **86**, 632 (2001).
[22] L. Kondic and J. Diez, Phys. Fluids **13**, 3168 (2001).
[23] L. Kondic and J. Diez, Phys. Rev. E **65**, 045301 (2002).
[24] L. Thomas, R. Gratton, B. Marino, S. Betelu, J. Diez, and J. Simon, Meas. Sci. Technol. **7**, 1134 (1996).
[25] R. R. E. L. W. Schwartz, J. Colloid Interface Sci. **202**, 173 (1998).
[26] L. W. Schwartz, Langmuir **14**, 3440 (1998).
[27] P. G. de Gennes, Rev. Mod. Phys. **57**, 827 (1985).
[28] R. Gratton, J. A. Diez, L. P. Thomas, B. Marino, and S. Betelú, Phys. Rev. E **53**, 3563 (1996).
[29] L. H. Tanner, Opt. Laser Technol. **10**, 125 (1978).
[30] M. F. G. Johnson, R. A. Schluter, M. J. Miksis, and S. G. Bankoff, J. Fluid Mech. **394**, 339 (1999).
[31] R. Goodwin and C. M. Homsy, Phys. Fluids A **3**, 515 (1991).
[32] B. M. Marino, L. P. Thomas, J. A. Diez, and R. Gratton, J. Colloid Interface Sci. **177**, 14 (1996).
[33] Y. Ye and H. Chang, Phys. Fluids **11**, 2494 (1999).
[34] P. Bloomfield, *Fourier Analysis of Time Series: An Introduction* (Clarendon, Oxford, 1976).
[35] L. M. Hocking, J. Fluid Mech. **221**, 373 (1990).